Journal of Applied Polymer Science

Preparation and properties of acrylonitrile-butadiene rubber-graphene nanocomposites

Bismark Mensah,[1] Dinesh Kumar,[2] Dong-Kwon Lim,[2] Seung Gyeom Kim,[1] Byeong-Heon Jeong,[3] Changwoon Nah[1]

[1]BK21 Plus Haptic Polymer Composite Research Team, Department of Polymer-Nano Science and Technology, Chonbuk National University, 567 Baekje-Daero, Jeonju 561-781, South Korea

[2]Department of BIN Fusion Technology, Graduate School of Engineering, Chonbuk National University, 567 Baekje-Daero, Jeonju 561-781, South Korea

[3]Fuel Cell Vehicle Team 1, Research and Development Division, Hyundai Motor Group, Yongin 446-912, South Korea

Correspondence to: C. Nah (E-mail: cnah@jbnu.ac.kr)

ABSTRACT: The graphene oxide (GO) was prepared by sonication-induced exfoliation from graphite oxide, which was produced by oxidation from graphite flakes with a modified Hummer's method. The GO was then treated by hydrazine to obtain reduced graphene oxide (rGO). On the basis of the characterization results, the GO was successfully reduced to rGO. Acrylonitrile–butadiene rubber (NBR)–GO and NBR–rGO composites were prepared via a solution-mixing method, and their various physical properties were investigated. The NBR–rGO nanocomposite demonstrated a higher curing efficiency and a change in torque compared to the gum and NBR–GO compounds. This agreed well with the crosslinking density measured by swelling. The results manifested in the high hardness (Shore A) and high tensile modulus of the NBR–rGO compounds. For instance, the tensile modulus at a 0.1-phr rGO loading greatly increased above 83, 114, and 116% at strain levels of 50, 100, and 200%, respectively, compared to the 0.1-phr GO loaded sample. The observed enhancement was highly attributed to a homogeneous dispersion of rGO within the NBR matrix; this was confirmed by scanning electron microscopy and transmission electron microscopy analysis. However, in view of the high ultimate tensile strength, the NBR–GO compounds exhibited an advantage; this was presumably due to strong hydrogen bonding or polar–polar interactions between the NBR and GO sheets. This interfacial interaction between GO and NBR was supported by the marginal increase in the glass-transition temperatures of the NBR compounds containing fillers. © 2015 Wiley Periodicals, Inc. J. Appl. Polym. Sci. **2015**, *132*, 42457.

KEYWORDS: composites; graphene and fullerenes; nanotubes; rubber

Received 9 March 2015; accepted 4 May 2015

DOI: 10.1002/app.42457

INTRODUCTION

Since the discovery of graphene by Geim, Novoselov, and coworkers,[1,2] a great deal of interest has been focused on its incorporation into polymer materials with the aim of preparing polymer–graphene-based nanocomposites.[3–6] Graphene is a flat monolayer of carbon atoms tightly packed into a two-dimensional honeycomb lattice with a completely conjugated sp^2 hybridized planar structure and is a basic building block for graphitic materials.[1,2] It is known that a single layer of graphene has extraordinary properties, including a Young's modulus of about 1 TPa, an ultimate strength of 130 GPa, a thermal conductivity of 5000 W m^{-1} K^{-1}), and an electrical conductivity of over 6000 S/cm. Moreover, graphene shows an extremely high surface area, flexibility, and transparency.[1,2,7]

For a better performance of polymer composites, one of the breakthrough technologies is a method of improving the exfoliation and dispersion of graphene and its derivatives (GRD) and creating stronger interactions with the polymer matrix through the proper introduction of functional groups on the surface of GRD. For this purpose, many researchers have considered using graphene oxide (GO), which is an exfoliated form of graphite oxide.[3,7,8] GO contains various functional groups, including epoxy (—O—C═O), hydroxyl (—OH), and carboxyl (C—O); this enables it to be dispersed effectively in polar and organic solvents and to bond well with polymer matrices. GO has been blended with different kinds of thermoplastics, thermosets, and elastomeric polymer matrices to enhance their mechanical, thermal, microwave absorption, and other properties. These polymers include polyurethane, polyester,[9,10] polyimide, epoxy,[11,12] and natural rubber (NR), ethylene–propylene–diene monomer, styrene–butadiene rubber, poly(dimethyl siloxane),[13–15] and more. The blending of GO into the polymer matrix has been

achieved largely by the common polymer processing techniques of melt mixing, solution blending, and *in situ* polymerization.[3,6,9–12]

Although GO shows advantages of better mixing and stronger interaction with polymers, it has been known that GO does not have electrical conductivity functionality because of its disrupted sp^2 hybridized bonds.[16] To attempt to recover its original honeycomb hexagonal lattice along with its electrical conductivity, a reduction process can be used to obtain a reduced form of GO called reduced graphene oxide (rGO).[16] Several reduction methods have been reported. These include exposure of GO to hydrogen plasma for a few seconds or to another form of strong pulse light by xenon flashtubes; the heating of GO in distilled water for different periods; the combination of GO with expansion–reduction agents, such as urea; and the heating of the solution to cause the urea to release reducing gases followed by cooling, direct heating of GO to very high levels in a furnace, and linear sweep voltammetry.[17–20] Among the reduction techniques, Hummer's and Brodie's methods are widely accepted for the large-scale production of graphenelike material (rGO), which is necessary for the preparation of polymer composites.[19–21]

Most of the works in the polymer–GRD nanocomposites are focused on the use of the GO;[9–11,22] this is probably due to its unique dispersion capability and interaction with polymers, notably thermoplastics and thermosets. There is little literature on elastomeric polymers.[23] Furthermore, polymer–graphene nanocomposites are hardly reported in the literature because of the difficulties of the proper dispersion associated with its reagglomeration tendency.[6,8–19,24] Thus, the residual amount of oxygen after reduction might contribute to the dispersion of graphene during the mixing process with polymers. A comparison of reinforcing behaviors between GO and rGO in a polymer matrix will be another challenging work in this field.

In this study, we synthesized GO by a modified Hummer's method[21] in the presence of prolonged sonication and reduced it to rGO by hydrazine. The fillers were then characterized to determine their basic characteristics with various analytical techniques. The composites based on a acrylonitrile–butadiene rubber (NBR) and GO and rGO were prepared via a solvent mixing route, which is known as be an effective way of dispersing nanosized fillers within a polymer matrix. NBR rubber was chosen because of its polar nature and its widely accepted unique oil resistance.[25] The state of dispersion of GO and rGO in NBR was studied with scanning electron microscopy (SEM), transmission electron microscopy (TEM), and wide-angle X-ray diffraction (WAXD). The tensile properties of the nanocomposites were obtained from stress–train curves, whereas the reinforcement behavior of GO and rGO in the NBR matrix were predicted by the Halpin–Tsai model. Other physical properties, such as hardness, crosslinking density, and thermal degradation behavior were also explored to fully understand the interactions of GO and rGO with the NBR matrix.

EXPERIMENTAL

Materials and Sample Preparation

Materials. NBR was supplied by Kumho Petrochemical Co. (Korea) under the trade name KNB 25LM with an acrylonitrile content of 20–30%. All chemical reagents [natural graphite (GR) flakes, hydrazine, and NH_4OH] were purchased from the Sigma-Aldrich (St. Louis, MO).

Table I. Compositional Formulation of the NBR–GO and NBR–rGO Compounds (phr)

Compound	NBR	ZnO	CZ	SA	TMTD	S	GO or rGO
NBR-GO-0.1	100	5	0.5	1.5	0.25	2	0.1
NBR-GO-0.5	100	5	0.5	1.5	0.25	2	0.5
NBR-GO-1	100	5	0.5	1.5	0.25	2	1
NBR-rGO-0.1	100	5	0.5	1.5	0.25	2	1
NBR-rGO-0.5	100	5	0.5	1.5	0.25	2	0.5
NBR-rGO-1	100	5	0.5	1.5	0.25	2	1

hr, parts per hundred of rubber; CZ, *N*-cyclohexyl-2-benzothiazolysulfenamide; TMTD, tetramethylthiuram disulfide; S, sulfur; SA, stearic acid.

Preparation of rGO. Graphite oxide was prepared by the oxidation of GR flakes according to the well-known modified Hummer's method;[21] these were then exfoliated by ultrasonication for a period of about 3 h to obtain GO. The GO obtained was then reduced by hydrazine assisted by NH_4OH. Briefly, after we obtained a powder of GO, 1 mL of hydrazine and 10 mL of NH_4OH were reacted with 200 mg of GO in 400 mL of water at a temperature of about 95°C for 1 h. The resulting solution was washed with water and centrifuged to obtain a gel of rGO. The gel was then freeze-dried to obtain a powdered rGO; this was used to process the compounds with NBR.

Preparation of the NBR Compound. The mixture of NBR and rGO or GO was prepared by a solution mixing process with the same conditions used in our earlier work for NBR–GO compounds.[23] The sulfur curing agents were added, mixed to obtain solid masses of NBR–rGO or NBR–GO compounds in a two-roll mill (Farrel 8422), and then sheeted out. A cure rheometer analysis was carried on the samples to determine the optimum curing conditions; this were used to cure the compounds by a hot press (Caver WMV50H) at a pressure of about 11 MPa and at 160°C with mold dimensions of 150 × 150 cm^2 and a 0.1-cm thickness. The samples were cut into standard shapes and subjected to further studies. Details of the compound formulations are given in Table I.

Characterization

X-ray Diffractometry (XRD). X-ray diffraction measurement (PaNalytical X'PERT powder diffractometer) was carried out to characterize the structures of GO, rGO, and their composites with Cu Kα radiation (40 kV, 100 mA, $\lambda = 0.154$ nm). X-ray diffraction patterns were obtained at room temperature with a scan step of 0.016711 (continuous type). The *d*-spacing of the particles was calculated with Bragg's equation.

Ultraviolet–Visible (UV–vis) Spectroscopy. A UV–vis spectrophotometer (S-3100, SINCO, South Korea) was used to obtain UV–vis spectra of both GO and rGO.

X-ray Photoelectron Spectroscopy (XPS). Characterization of GO and rGO were done with an XPS instrument (model AXIS-NOVA, Kratos, Inc.).

Raman Spectroscopy. The structural analyses of GR, GO, and rGO were performed by Raman spectroscopy (Renishaw, Raman Micro System 2000, Derbyshire, United Kingdom) with a 633-nm wavelength laser.

Fourier Transform Infrared (FTIR) Spectroscopy. FTIR spectra of GO and rGO were recorded on a Jasco FTIR-4200 spectrophotometer.

SEM. The morphologies of the rGO and GO powders and the cryogenically fractured surfaces of their compounds, NBR–rGO and NBR–GO, were coated by platinum via sputtering and then observed with field emission SEM (JEOL, JSM 599, Japan).

TEM. Solutions of rGO/dimethyl furan and GO/dimethyl furan were gently dropped onto TEM 200-mesh copper grids and allowed to dry. The TEM images of these nanoparticles were taken and examined. Also, ultrathin NBR, NBR–rGO, and NBR–GO specimens (thinner than 100 nm) for TEM observation were cryogenically cut with a diamond knife with an ultramicrotome (Leica Ultracut CUT, Germany) and collected on 200-mesh copper grids. The dispersion of the rGO and GO nanosheets in NBR rubber was separately observed with TEM (JEOL, JEM2100, Japan), and the distribution of rGO and GO within the NBR matrix was analyzed.

Thermogravimetric Analysis (TGA). Differential scanning calorimetry (DSC)–TGA (TA Instruments, SDT Q600 V20.9 Build 20) was used to investigate the thermal degradation behavior of rGO and GO and their compounds with NBR. The conditions included a nitrogen medium, an equilibrium temperature of 30°C, and a heating rate of 10°C/min to a maximum temperature of 800°C.

DSC. The glass-transition temperature (T_g) of the compounds was investigated with DSC (Universal V4.7A, TA Instruments, Q20 V24.9 Build 121). All samples were cooled to −80°C at 10°C/min and reheated up to 80°C at 10°C/min.

Tensile and Hardness Testing. The tensile strength measurements of the specimens were carried out according to ASTM D 412 with a Lloyd instrument (United Kingdom) with a dumbbell-shaped specimen. The specimen was subjected to a stress–strain test at a crosshead speed of 500 mm/min at room temperature. The tensile properties (elongation, modulus, and tensile strength) were deduced from the stress–strain curve. At least four samples were tested for each composition, and these values were averaged.

Crosslinking Density by Swelling. Swelling experiments of the cured compounds were performed by the equilibration of the samples (NBR–GO and NBR–rGO) in methyl ethyl ketone (MEK) with a molar volume of 72.11 mL/mol at room temperature for 72 h. Initially, the sample dimensions were estimated, and the sample weight was w_1. The sample was then immersed into the solution; after immersion, the soaked sample was wiped and weighed to obtain the swollen weight (w_2). This step was repeated until equilibrium was reached. The equilibrium swollen weight and the weight of the liquid absorbed at a certain time ($W_l = w_2 - w_1$) were recorded. The swelling degree (Q) was calculated with eq. (1):

$$Q = \frac{(W_s/\rho_s)+(W_l/\rho_l)}{(W_s/\rho_s)} \quad (1)$$

where W_s is the weight of the specimen and ρ_s and ρ_l are the densities of the solid specimen and the liquid, respectively. The crosslinking density (n) was then calculated with the Flory–Rehner model:[26]

$$n = \frac{-\left[\ln(1-v_2)+v_2+\chi_1 v_2^2\right]}{V_1\left(v_2^{1/3}-\frac{v_2}{2}\right)} \quad (2)$$

where v_2 is the volume fraction of the polymer in a swollen gel at equilibrium and is given by $1/Q$ and V_1 is the molar volume of MEK. The interaction parameter (χ_1) between NBR and MEK was 0.342 on the basis of the Bristow–Watson equation:[27]

$$\chi_1 = \beta_1 + \left(\frac{v_s}{RT}\right)(\delta_s-\delta_p)^2 \quad (3)$$

where β_1 is the lattice constant (typically, 0.34), v_s is the volume of solvent per molecule, R is the gas constant, and T is the absolute temperature. The solubility parameter of NBR (δ_p) and the solubility parameter of the solvent MEK (δ_s) were 9.29 and 9.27 $(\text{cal/cc})^{1/2}$, respectively.

Dielectric Constant (k). The k values of the representative samples (NBR, NBR–GO, and NBR–rGO compounds) were measured by a meter (VHR-200). The conditions used include the following: 0 V, frequency = 1–1000 KHz, and step frequency = 1 KHz (optimum conditions for the samples in this study). Each side of the specimen was coated with conductive silver grease to improve the electrical contact between the specimens and the electrodes. The amount and number of silver coatings was maintained at the same rate and thickness to prevent variations in the thickness of the samples. The average thickness of the samples was about 1.2 mm. All of the measurements were carried at room temperature.

RESULTS AND DISCUSSION

Characterization of GRD

Morphology and Physical Structure. ***SEM and TEM analysis.*** Graphite possesses a layered crystalline structure with interlayer spacing of about 0.34 nm.[7,16,24,28] After oxidation and exfoliation, GO showed a kind of amorphous structures with structural imperfections such as wrinkles [Figure 1(a)]. The reduction of GO by hydrazine lessened the structural deformation, as shown in Figure 1(b). Both the GO and rGO sheets appeared to be transparent sheets with wrinkled structures with a thickness of 0.83–2 nm, as shown by the TEM images in Figure 1(c,d).

XRD analysis. Figure 2 shows the XRD pattern of the fillers (GR, GO, and rGO). A sharp diffraction peak was observed at $2\theta = 26.5°$ (with a corresponding d-spacing of 0.34 nm) for crystalline graphite; this indicated a tightly layered structure. The GO peak at an angle of 10.2° (with a corresponding d-spacing of 0.87 nm) indicated the inclusion of oxygen moieties into the galleries and water molecules held in the interlayer galleries of the hydrophilic GO. Similar results were reported earlier.[6,29,30] Upon reduction of GO, the peak became extremely

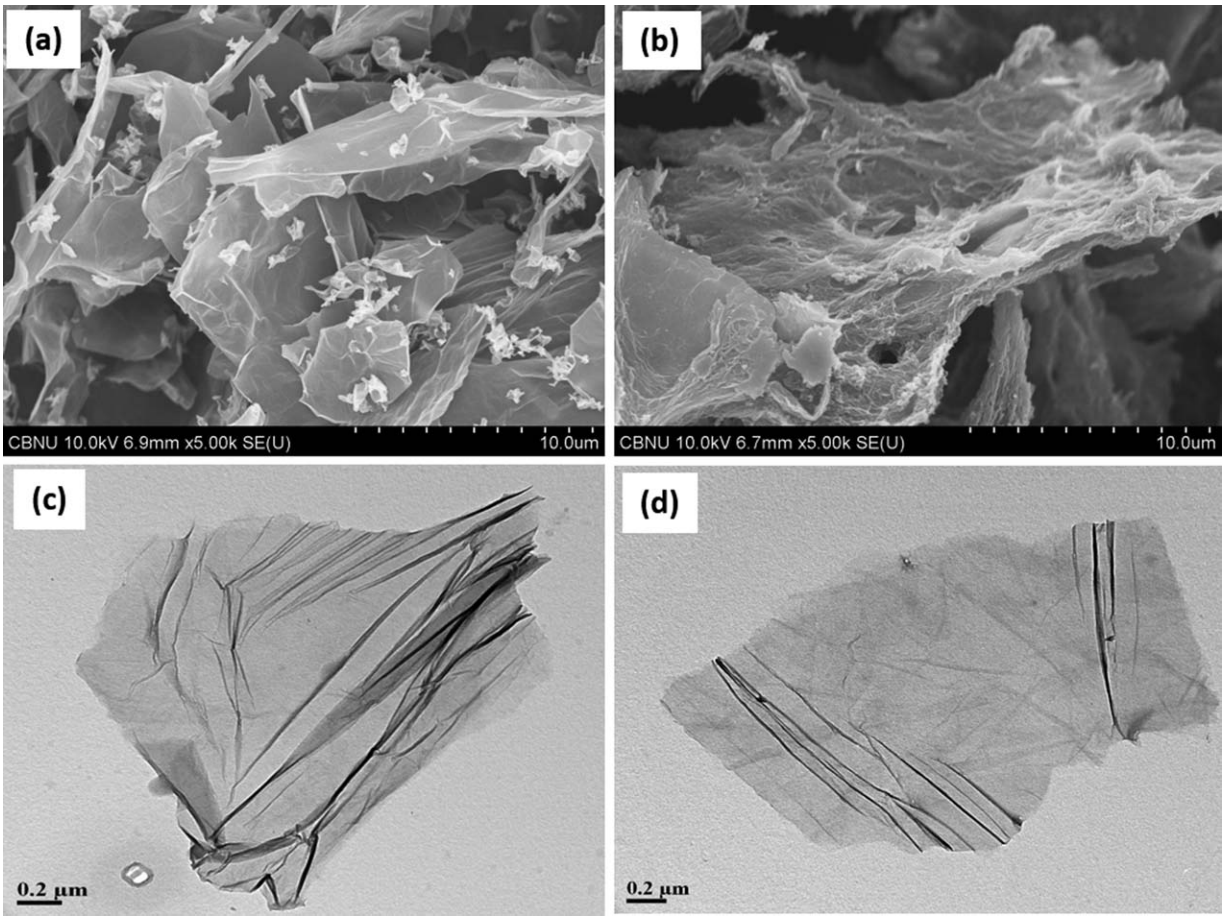

Figure 1. Morphological shape of GO and rGO: SEM images of (a) GO and (b) rGO and TEM images of (c) GO and (d) rGO.

broader, as shown in Figure 2. This indicated that the rGO layers were in an almost exfoliated state.

Chemical Structure. ***FTIR analysis.*** The FTIR spectra of GO and rGO are presented in Figure 3(a). The broad absorption band, which was due to the O—H stretching vibration, and the absorbed water molecules was observed in a high-frequency region around 3000–3700 cm^{-1} for GO; this showed the hydrophilic nature of GO.[30] The C═O stretching vibrations of the COOH groups located at the edges of the GO sheets were seen at 1742 cm^{-1}. The stretching vibration peaks of C—O (epoxy) and C—O (alkoxy) were observed at 1219 and 1039 cm^{-1}, respectively. The peak marked 1621 cm^{-1} was assigned to the vibrations of the adsorbed water molecules and also the contributions of the skeletal vibrations of unoxidized graphitic domains.[30,31] The marked observation here was that after the reduction of GO, most bands corresponding to the oxygen-containing functional groups, such as hydroxyl, epoxy, and alkoxy, vanished, or the intensity was significantly reduced, as shown in the spectrum of rGO. This strongly supported the occurrence of a reduction in rGO. The peak at 1576 cm^{-1} was attributed to the skeletal vibrations of the graphene sheets.[30] It should be noted here that GO was not completely reduced to pristine graphene; this indicated the presence of some residual oxygen-containing groups in rGO.[32,33] The residual functional groups might have been useful in the rubber compounding via additional bond formation.

Raman spectroscopy. Figure 3(b) shows the Raman spectra of the GR, GO, and rGO. This technique is known to be a powerful tool for quantifying the transformations from sp^3 to sp^2

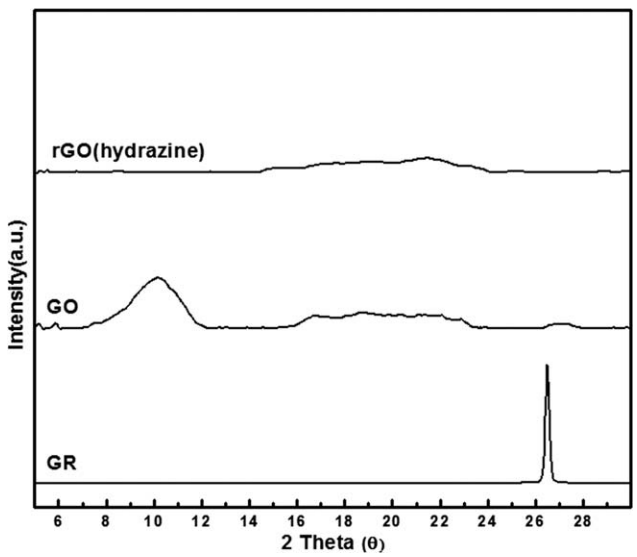

Figure 2. XRD spectra of GR, GO, and rGO.

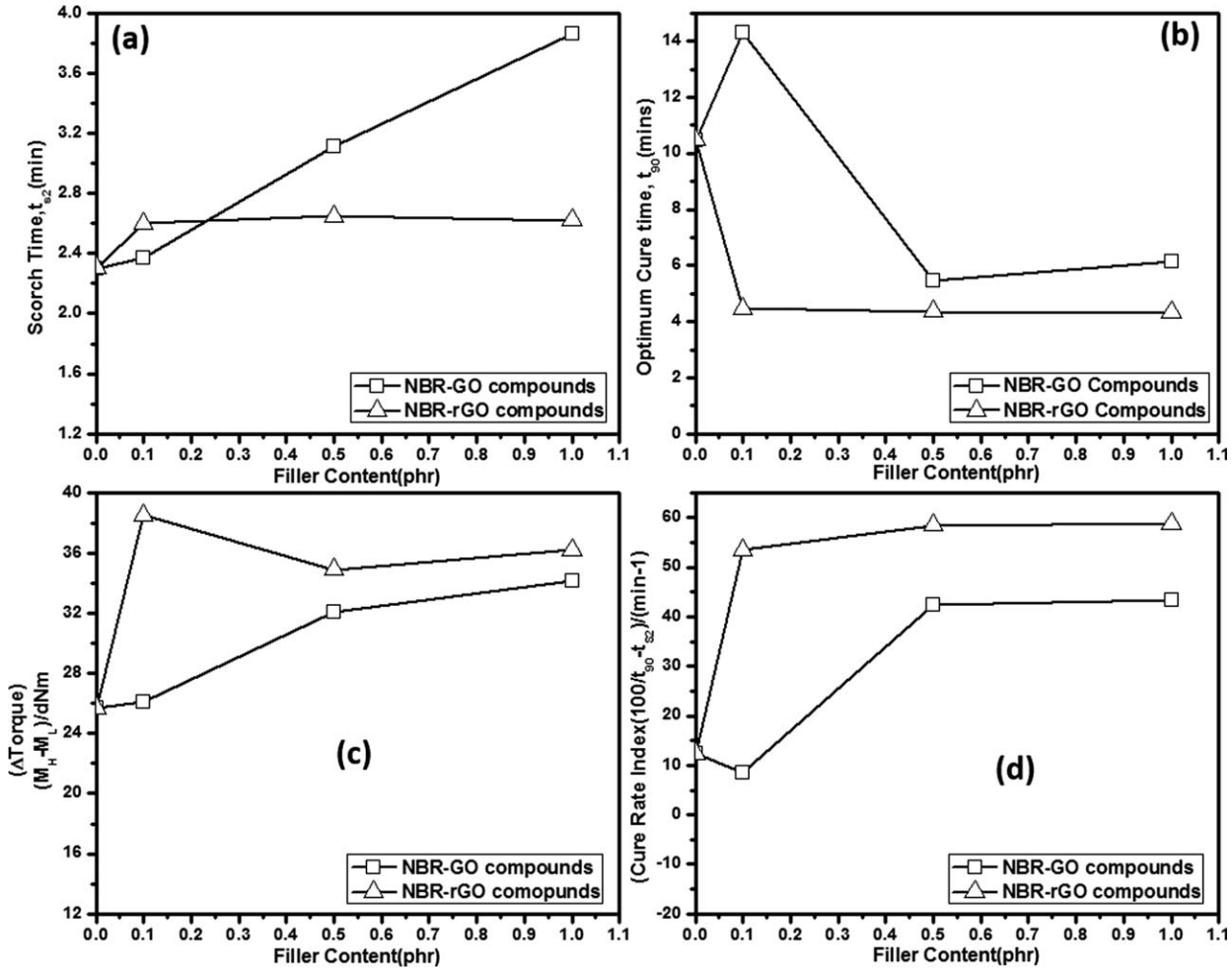

Figure 3. Chemical characterization of GRD: (a) FTIR spectra of GO and rGO; (b) Raman spectra of GR, GO, and rGO; and XPS spectra of (c) GO and (d) rGO.

hybridization through the intensity in the variation of bands in the spectrum. The D band (associated with the order–disorder of the system) and the G band (an indicator of the stacking structure) are the dominant vibrational modes observed in the graphitic structures.[6,7,34] The ratio of the intensities of the two bands (D/G) is often used as a means of determining the number of layers in a graphene sample and its overall stacking behavior. High D/G ratios indicate a high degree of exfoliation–disorder.[7,34,35] As shown in Figure 3(b), both the spectra of GO and rGO show the existence of the D and G band. For GO, the G band was located at 1592 cm^{-1}, whereas for rGO, it shifted to 1586 cm^{-1}; this corresponded to the value of pristine graphene (1586 cm^{-1}). The increase in the intensity ratio of the D and G bands (I_D/I_G), from 0.3 for graphite to 1.04 for GO to 1.37 for rGO, is generally evidence of the successful chemical reduction of GO to rGO.[7,34] At the same time, there exists D bands for the two spectra, which are located at 1337 and 1331 cm^{-1} for GO and rGO, respectively. These peaks correspond to a defect of the sample and the size of the in-plane sp^2 domain.[34]

XPS analysis. We also adopted XPS analysis[7,34,36] to characterize the GO and rGO. The results are presented in Figure 3. The ratio of carbon to oxygen (C/O) was calculated from the atomic concentrations (oxygen and carbon) in both the GO and rGO spectra, and this is summarized in Table II. It was interesting to note that C/O increased from 1.95 to 4.81 for GO and rGO, respectively. This indicated evidence of the deoxygenation of GO and the formation of rGO. Furthermore, Figure 3(c,d) can be decomposed into several symmetrical components, where C_{1s} had four peaks and O_{1s} had two peaks.[6,37] The most intense peak between 284.6 and 285.8 eV in the C_{1s} spectrum was assigned to the sp^2 and sp^3 carbon atoms, whereas the peaks in the regions 286.3–286.5 and 288.0–289.0 eV corresponded to the C—O—C and —O—C═O functional groups, respectively.[6,37] Meanwhile, the O_{1s} spectrum was also used as a complement for the C_{1s} spectrum because it is known that some difficulties might arise in the correct assignments of the functional groups on graphene.[6,37] Thus, the deconvolution of the O_{1s} spectrum will yield two peaks: (1) one at 531.5 eV corresponding to —O—C═O groups and (2) one between 533.5 and 533.9 eV assigned to the C—O—C groups. As shown in Table II, the regular O_{1s} and C_{1s} peaks in our study for the GO spectrum were observed at 535.70 eV (—O—C═O) and 290.350 eV (—O—C═O), respectively, as shown in Figure 3(c). Similarly

Table II. XPS Analysis Data of the Solid GO and rGO Particles

	Peak	Type	Position (eV)	fwhm (eV)	Raw area (cps eV)	Atomic mass	Atomic concentration (%)	Mass concentration (%)
GO	Na1s	Reg	1074.650	1.656	3,454.1	22.990	0.56	0.93
	O1s	Reg	535.700	3.023	90,839.1	15.999	31.92	36.67
	N1s	Reg	404.750	3.027	4,083.6	14.007	2.36	2.38
	C_{1s}	Reg	290.350	4.489	62,512.1	12.011	62.31	53.74
	C_{2p}	Reg	201.850	2.231	1,250.9	35.460	0.39	1.00
	S_{2p}	Reg	171.550	2.211	2,356.7	32.065	0.98	2.27
	Si_{2p}	Reg	104.750	2.042	1,659.0	28.086	1.46	2.95
	Au_{4f}	Reg	85.850	0.433	110.4	196.967	0.01	0.07
rGO	Na_{1s}	Reg	1071.550	1.720	3,542.7	22.990	0.68	1.17
	O_{1s}	Reg	532.100	2.711	37,969.6	15.999	15.79	18.87
	N_{1s}	Reg	399.900	2.281	7,192.7	14.007	4.92	5.15
	C_{1s}	Reg	284.800	1.578	64,451.4	12.011	76.02	68.21
	C_{2p}	Reg	198.350	1.145	1,127.2	35.460	0.42	1.10
	S_{2p}	Reg	168.950	0.071	60.0	32.065	0.03	0.07
	Si_{2p}	Reg	101.750	1.622	1,983.6	28.086	2.08	4.36
	Au_{4f}	Reg	84.450	1.177	1,305.0	196.967	0.07	1.07

fwhm, full width at half-maximum.

the regular peaks (O_{1s} and C_{1s}) for the rGO spectrum were observed around 532.10 eV (C—O—C) and 284.80 eV (C—C), respectively, as shown in Figure 3(d). It should be noted here that although the rGO also showed an oxygen-related XPS spectrum, the peak intensity was much smaller than that of GO.

UV–vis spectroscopy. The UV–vis spectra of GO and rGO are shown in Figure 4. We observed that GO exhibited a maximum absorption peak at about 225 nm; this corresponded to the optical absorption of GO at the π–π^* plasmon peak. This peak shifted to 271 nm for rGO. According to Lai *et al.*,[38] the π–π^* plasmon peak depends on two kinds of conjugative effects: one is related to nanometer-scale sp^2 clusters, and the other arises from linking chromophore units, such as C=C, C=O, and C—O bonds. We assumed that a reduction of GO into rGO by hydrazine would result in mainly C=C bonds and a reduced amount of oxygenated functional groups. The observed peak shift was suggested as a tool for measuring the level of reduction of GO into rGO.[30,39] Additionally, the shoulder peak of GO, which seemed to appear at about 300 nm, was due to the n—π^* transitions of aromatic C=O bonds,[30,38] but this was absent in the rGO spectrum.

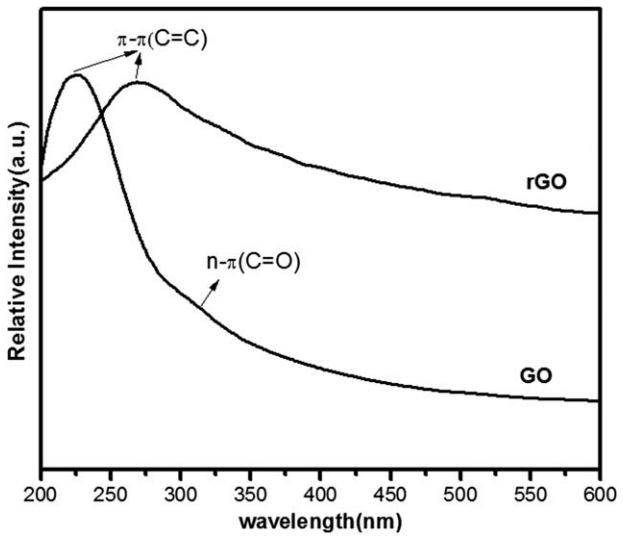

Figure 4. UV–vis spectra of GO and rGO.

Thermal stability. Table III shows the TGA thermograms of GO and rGO. The initial degradation temperatures [defined as the temperatures showing a 10% weight loss (T_{10}'s)] of GO and rGO were seen between 103.7 and 198.5°C. The extensive initial degradation for GO was ascribed to the evaporation of CO, CO_2, and water. The total weight losses of GO and rGO after major decomposition at about 800°C were 48.0 and 69.6%, respectively. The improved thermal stability of rGO was credited to the low level of oxygen-containing groups,[40] and this was expected to improve the thermal stability of the respective composites.

Characterization of the Nanocomposites. ***Curing characteristics.*** In our previous study,[23] we observed that the incorporation of GO into NBR delayed the scorch time (t_{s2}) but reduced the optimum cure time (t_{90}), and thus, a faster cure rate was seen. Similar behavior was reported in functionalized multiwall

Table III. Thermal Degradation Stability of GO and rGO

Filler	T_{10}	T_{90}	Weight residue (%)
GO	103.7	>796	48.0
rGO	198.5	>800	69.4

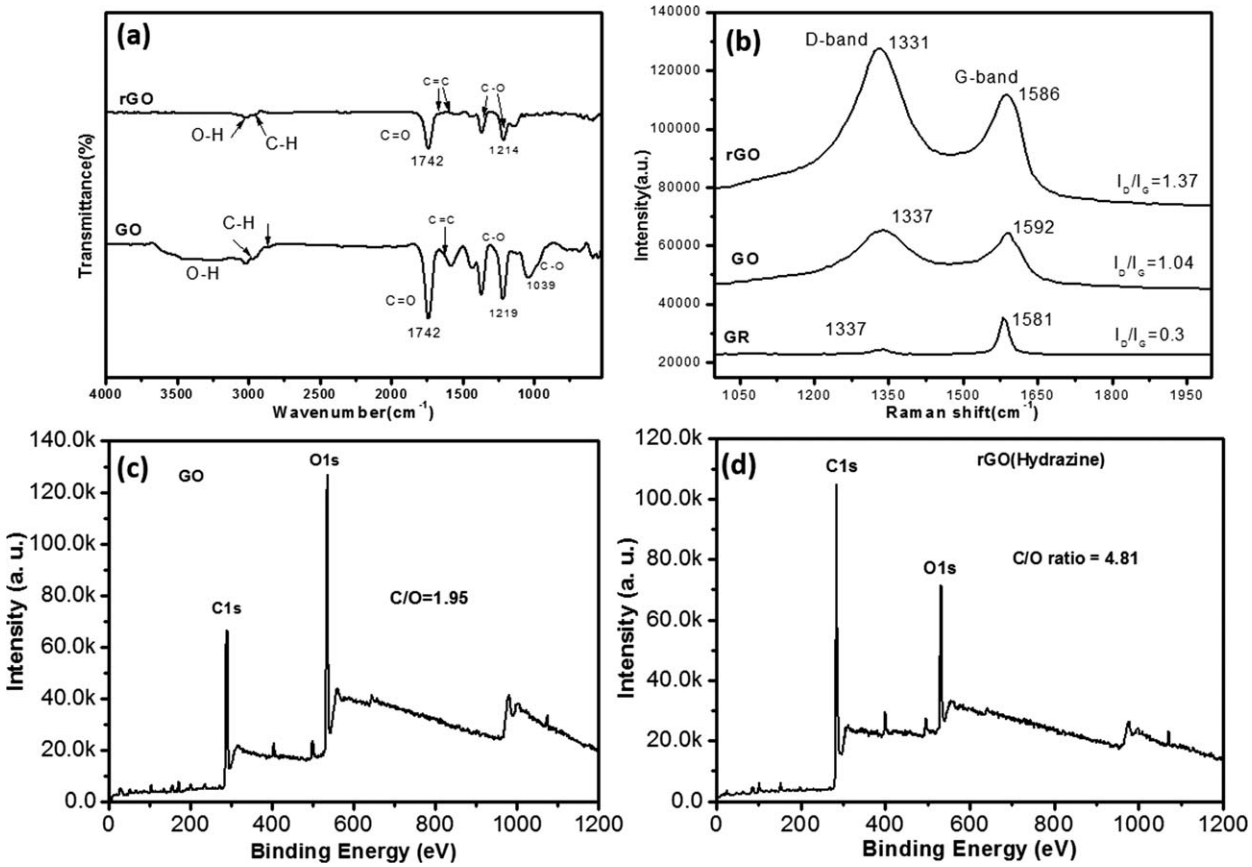

Figure 5. Curing properties of the NBR–GO and NBR–rGO compounds: (a) t_{s2}, (b) t_{90}, (c) ΔTorque, and (d) CRI.

carbon nanotube–NR and GO–epoxy systems.[41,42] The initial delay in t_{s2} was assigned to the absorption of a cure accelerator by the oxygen-containing groups on the surface of the GO nanoparticles. It was interesting to explore the effect of rGO (with much less oxygen-containing groups) on the curing behavior of their corresponding nanocomposites. The major curing properties, including t_{s2}, t_{90}, torque difference ($\Delta\text{Torque} = M_H$ (maximum) $- M_L$ (minimum)), and cure rate index [$\text{CRI} = 100/(t_{90} - t_{s2})$], of the NBR–rGO compounds were deduced from the curing curves at $T = 160°\text{C}$, and they are plotted in Figure 5 for a comparison with NBR–GO compounds. The t_{s2} values for the NBR–rGO compounds were found to remain almost constant [Figure 5(a)]. This strongly supported the reduction of the oxygen-containing groups on the surface of the rGO particles. A further decrease in t_{90}, which led to a faster CRI, was observed among the NBR–rGO compounds, as shown in Figure 5(b,d). Moreover, a greater enhancement in ΔTorque, which corresponded to the relative crosslinking density of the samples, was observed for the NBR–rGO compounds, notably at a lower rGO loading [0.1 phr; Figure 5(c)]. This result was in a good agreement with the crosslink density measurement by swelling shown in Table IV; this is discussed in a later section. The improvement in ΔTorque seemed to be the cause of the better dispersion and exfoliation of rGO fillers in the NBR matrix and the stronger interaction between the rGO and NBR chains. It is worth mentioning here that the formation of additional chemical crosslinks between electron acceptor groups in the acrylonitrile group of NBR and the residual oxygen functionalities on the rGO surfaces was possible. Typically, the residual hydroxyl (—OH) group attached to the edges of rGO is known to be an electron-donating group and can, therefore, bond adequately with NBR.[22,29] However, the increase in ΔTorque leveled off above 0.1 phr of rGO content; this was possibly due to clustered rGO sheets in the NBR matrix, as shown schematically in Figure 6. Insight into the

Table IV. Some Physical Properties of the NBR, NBR–GO, and NBR–rGO Compounds

Samples	Hardness (Shore A)	Crosslinking density × 10^{-4} (mol/cm^3)	T_g (°C)
NBR	52.0 ± 0.80	4.89	−42.1
NBR-GO-0.1	53.8 ±0.94	3.87	−41.1
NBR-GO-0.5	56.0 ± 0.18	—	—
NBR-GO-1	56.7 ± 0.62	5.43	−41.3
NBR-rGO-0.1	57.3 ± 0.35	6.10	−41.8
NBR-rGO-0.5	58.5 ± 0.46	—	—
NBR-rGO-1	59.8 ± 0.35	5.80	−41.3

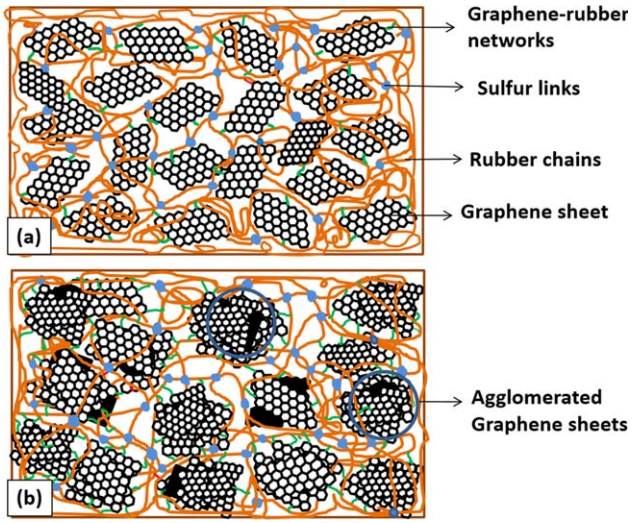

Figure 6. Schematic representation of the state of dispersion of GRD in a rubber matrix: (a) ideally dispersed single-layer sheet and (b) agglomerated sheets. [Color figure can be viewed in the online issue, which is available at wileyonlinelibrary.com.]

curing kinetics of the NBR–GO and NBR–rGO nanocomposites will be a fascinating area of study in the future.

Morphology and dispersion of the fillers. The morphologies and states of dispersion of the GO and rGO fillers in the NBR matrix were investigated by SEM and TEM, and they are shown in Figure 7. Deeply embedded GO and rGO sheets in the NBR matrix were not initially observed on the matrix surface by the SEM technique. Thus, a compressive stress was applied to the sample; this made sheets come out to the observed surfaces. The detailed procedure was explained in our previous works on carbon-nanotube-reinforced rubber compounds.[43,44] As shown in Figure 7(a,b), both the composites contained some small degree of wrinkled protrusions of nanosheets; these created surface roughness. Clearly, the wrinkled protrusions and surface roughness of the NBR–rGO composites seemed to be slightly more intense than those of the NBR–GO composites. The wrinkled surface texture of the GO and rGO sheets in the composites has been reported to play an important role of mechanical interlocking and load transfer in polymer composites.[6,45,46] A similar texture of graphene was observed by Rafiee and coworkers,[45] who reinforced epoxy with functionalized graphene sheets (FGS).

In addition, TEM images of the compounds in Figure 7(c–f) represent the dispersion state of the GO and rGO sheets at different loadings in the NBR matrix. As shown in Figure 7(c,d), the rGO seemed to be evenly dispersed in the NBR matrix at all filler loading levels (0.1–1 phr) compare to GO, as shown by black arrows. However, some cluster formations of nanosheets were seen at higher filler loading levels (1 phr) in both the NBR–rGO and NBR–GO composites (encircled with a dotted white color), as shown in Figure 7(e,f), respectively. However, the agglomerates in NBR–rGO-1 appeared to be more vigorous than those of NBR–GO-1. The successful dispersion of rGO in the NBR matrix, especially at lower filler concentrations, was the effect of the enhanced torque values of the NBR–rGO compounds and it likely influenced the other physical properties of composites.

Crosslinking density. The results of the crosslink density of the samples measured by the swelling method are shown in Table IV. Generally, the crosslinking densities of the nanocomposites were higher than that of the gum, although oxygen groups present in both GO and rGO particles were believed to be responsible for chemical crosslinks in the composites. The chemical interaction in both NBR–GO and NBR–rGO compounds, which occurred between the electron-acceptor groups of acrylonitrile in the NBR and the electron-donating hydroxyl groups on the GO or rGO surfaces[22,29] was ideally anticipated to be much greater in the NBR–GO compounds than in the NBR–rGO specimens. Such interactions were due to hydrogen bonding.[16,29,47] Perhaps, the better dispersion of rGO sheets in the NBR matrix, which led to more physical crosslinks between the rGO and NBR molecules, might have caused the marginally higher densities in the NBR–rGO compounds than in the NBR–GO compounds. This result matched well with the crosslinking density (ΔTorque) calculated form the cure curve [Figure 5(c)]. A further study will be necessary to establish the interaction between the filler and rubber matrix because these interactions are closely related to the physical properties of the bulk compounds.

Tensile properties and hardness. The stress–strain curves of the NBR, NBR–GO, and NBR–rGO compounds are shown in Figure 8. The incorporation of GO or rGO into the NBR matrix mostly enhanced the tensile properties compared to the pure matrix, even though the filler loading was extremely low; this indicated a characteristic feature of the polymer nanocomposite. It was very interesting to note here that the NBR–rGO compounds showed the highest enhancement in modulus at all filler loadings. At a 0.1-phr rGO loading, the tensile moduli at 50, 100, and 200% strains were increased by 83, 114, and 166%, respectively, relative to the neat NBR rubber. However, a higher rGO content was observed to lessen the tensile modulus because of a possible formation of agglomerates, as depicted in Figure 6. The significant enhancement in stiffness for the NBR–rGO compounds was also confirmed by the hardness (Table IV). The level of improvement in stiffness was noticeably higher compared with those found in other works, including NBR–rGO,[48] hydrogenated carboxylated NBR–GO,[29] and NR-functionalized graphene.[6]

On the other hand, the ultimate strengths [tensile strength at break (σ_b) and elongation at break (ε_b)] of NBR–GO compounds were generally higher than those of the NBR–rGO compounds. For example, σ_b of NBR–GO-0.1 was about 36% greater than that of NBR–rGO-0.1. Such development was attributed to the strong chemical interaction between NBR and GO, as already explained. An increase in T_g of the NBR–GO compounds was used to support the strong interfacial bonds existing between NBR and GO. More reports on the interactions between GRD and polymers are available in the literature.[6,29,42,48]

Reinforcing behavior. The reinforcing effect was analyzed by the ratio of the moduli between the composite and the matrix polymer, and they were compared with the Halpin–Tsai equation:[49]

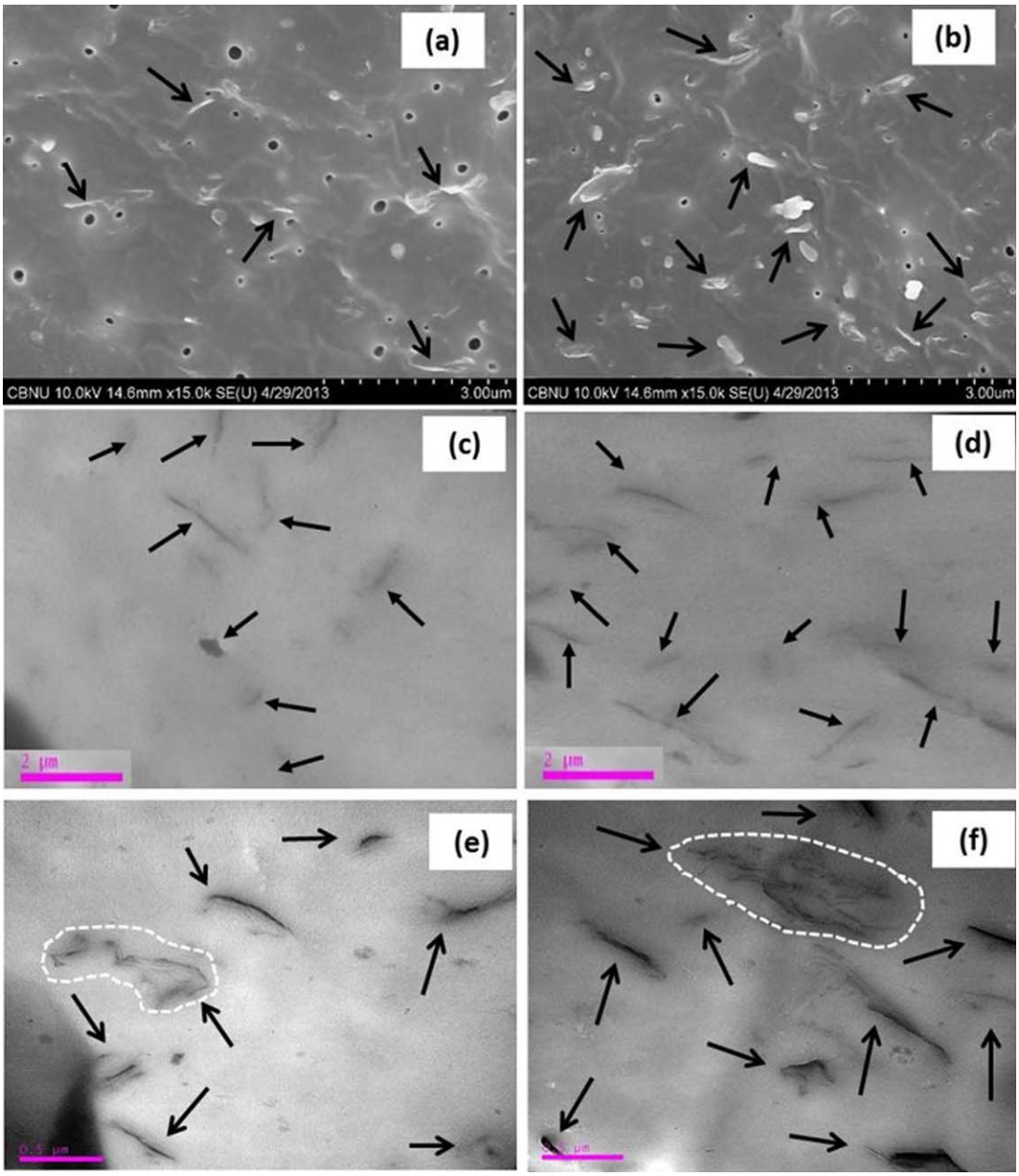

Figure 7. Morphology and state of dispersion of the compounds: SEM images of (a) NBR–GO-0.1 and (b) NBR–rGO-0.1 and TEM images of (c) NBR–GO-0.1, (d) NBR–rGO-0.1, (e) NBR–GO-1, and (f) NBR–rGO-1. [Color figure can be viewed in the online issue, which is available at wileyonlinelibrary.com.]

$$\frac{E_c}{E_m}=\frac{(1+V_p\zeta\eta)}{(1-V_p\eta)}. \quad (4)$$

$$\eta=\frac{(E_c/E_m-1)}{(E_c/E_m+\zeta)} \quad (5)$$

where E_c and E_m are the moduli of the composites and the matrix, respectively, and V_p (%) and ζ are the volume fraction and shape parameter of the filler (1015 for GO and 1049 for rGO in this study), respectively. Given the densities of NBR, GO, and rGO of 1.3, 2.28, and 1.91 g/cm^3,[21,24,25,50] respectively, the V_p values of the fillers in the rubber compounds were calculated. The experimental data for E_c/E_m were taken as the tensile modulus at 200% elongation (σ_{200} in Figure 8), and they were plotted as a function of V_p along with the fitted curve with the Halpin–Tsai model (Figure 9). There was a quite good agreement between the experimental data and the theoretical predictions for the NBR–GO compounds. In contrast, the experimental values for the NBR–rGO compounds greatly exceeded the theoretical prediction, especially at a lower V_p (0.07%) of rGO. This strongly supported the theory that the superior reinforcing behaviors of rGO compared with GO in terms of stiffening was responsible for the better exfoliation and dispersion of rGO. It has been reported that the performance of polymer nanocomposites is strongly affected by both the

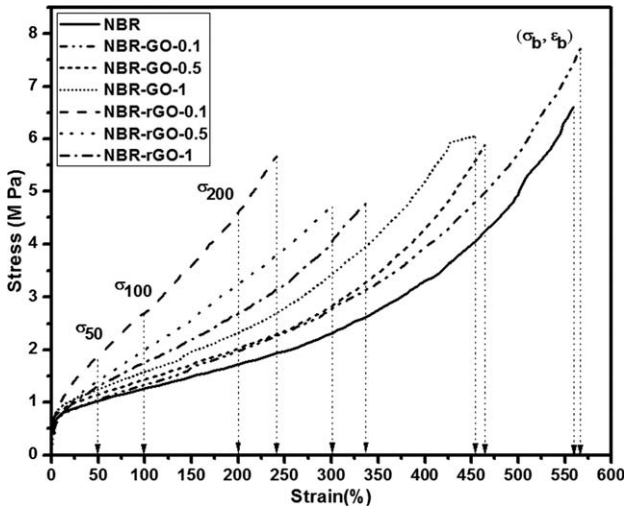

Figure 8. Stress–strain curves of the NBR, NBR–GO, and NBR–rGO compounds.

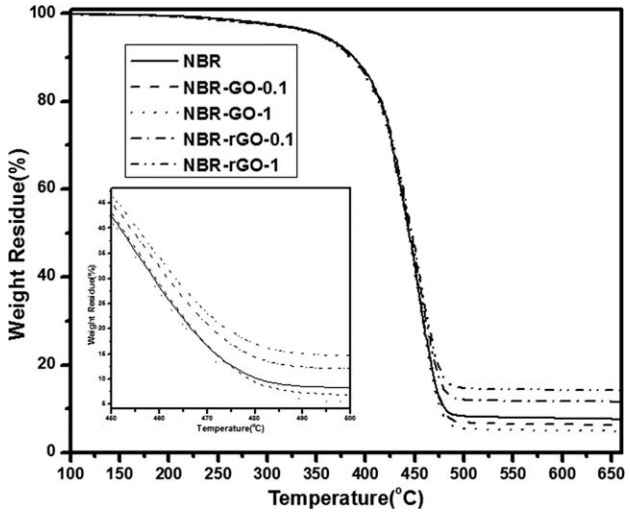

Figure 10. TGA thermograms of the NBR, NBR–GO, and NBR–rGO compounds.

orientation[51] and dispersion of nanosized fillers[3–6,8] and structural imperfection, especially for GRD fillers.[22,24,29,30,45,52]

T_g. The T_g values of NBR, NBR–GO, and NBR–rGO compounds are given in Table IV. The T_g of NBR was observed at −42.09°C. The incorporation of rGO and GO slightly increased the T_g values of the composites compared to that of the gum. This could have been due to the restriction of molecular motions of rubber chains bonded with sheetlike particles decorated with oxygen functionalities.[6,29,42,48] The effect seemed to be stronger for the NBR-GO compound because of stronger chemical interactions between the GO and NBR matrix, as reported in the literature.[48]

Thermal stability. The thermal degradation properties (TGA) of the pure NBR and composites are shown in Figure 10. The degradation temperatures were taken at two different levels of degradation, 5 and 90%, and these temperatures are represented as T_5 and T_{90}, respectively. The initial (T_5) and maximum (T_{90}) degradations were observed at about 350 and 450°C, respectively, for all of the compounds. However, a considerable difference was found for the weight residues among the samples. Generally, the NBR–rGO compounds showed higher values of weight residues. This could be explained by two causes: one was the better thermal stability of the rGO fillers themselves, and the other was the higher potential of char formation. Enhanced char formation was recently reported for polymer–graphene nanocomposites, and it was higher than that of the GO fillers. This suggested an incredible improvement in the thermal stability of the NBR–rGO compound in this study.[16]

k. The k values of the neat NBR and representative composites (NBR–GO-0.5 and NBR–rGO-05) are presented in Figure 11. It has been suggested that the incorporation of GO gives rise to higher k values because of a possible enhancement in the electric conductivity and more significant interfacial polarization (IP; the accumulation of unlocked charges at an interface).[23] In

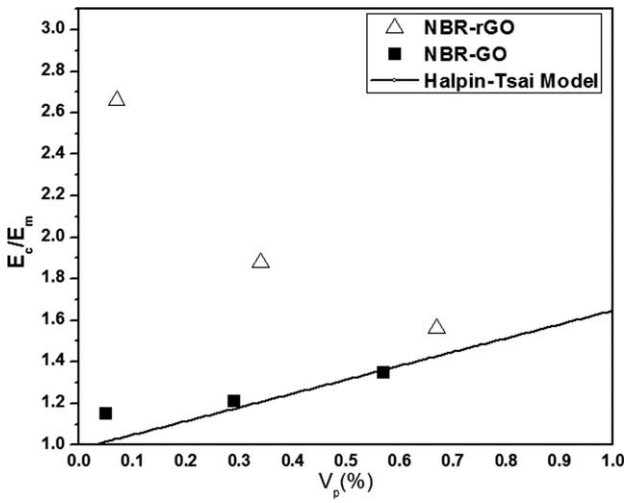

Figure 9. Modulus ratio (E_c/E_m) of the NBR–GO and NBR–rGO composites a function of V_P.

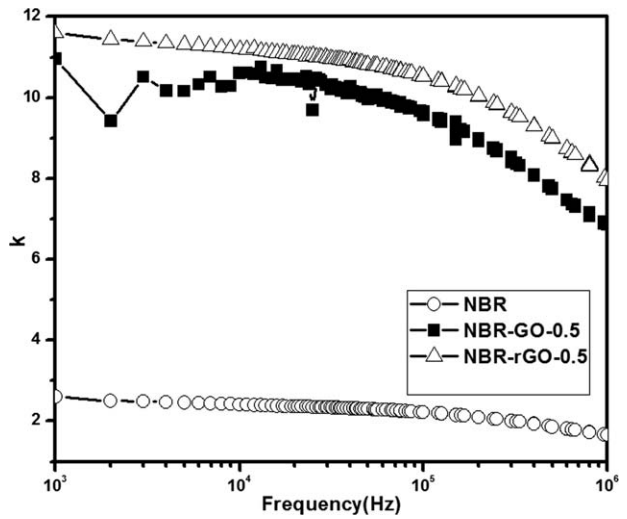

Figure 11. k values of the NBR, NBR–GO-0.5, and NBR–rGO-0.5 compounds as a function of the frequency.

this study, the k value appeared to be even higher for the NBR–rGO compounds; this may have proven the restoration of the electrical conductivity of GO after reduction to rGO. It is also known that the intensity of IP provides indirect evidence of the good distribution of nanofillers in a polymer matrix.[54] Thus, the better dispersion of rGO in the NBR matrix was again supported by the high values of k. Another point to be mentioned here was the strong dependence of the frequency on the k values. For instance, the remarkable difference in IP-induced k values among compounds at lower frequency regions became smaller because of the competition of the higher electrical field and the increased frequency.[55]

CONCLUSIONS

On the basis of physical analyses (SEM, TEM, XRD, and TGA) and chemical analyses (FTIR, Raman, XPS, and UV–vis), it was confirmed that rGO and GO were successfully synthesized from graphite flakes via a modified Hummer's method and chemical treatment by hydrazine.

When the rGO was used in the NBR matrix, noticeable improvements were observed in the CRI, crosslink density, k, and stiffness compared with those of the NBR-GO compounds. The improvement was generally observed at a lower loading level of rGO (~0.1 phr). This was ascribed to the improved exfoliation and dispersion of rGO in the NBR matrix at a lower concentration of rGO; this was evidenced by the SEM and TEM morphologies. At higher loading levels, a trend of clustering of rGO was observed.

The NBR–rGO compounds, however, showed inferior ultimate strengths, such as σ_b and ε_b, when compared with the NBR–GO compounds. This was explained by the relative level of chemical interaction between the oxygen-containing groups of GO and rGO and acrylonitrile groups in the NBR matrix. The surface of GO was covered with plenty of functional groups, including carboxylic, epoxy, carbonyl, and hydroxyl groups, which could interact with NBR hydrogen bonding or polar–polar interactions.

ACKNOWLEDGMENTS

This work was supported by both BK 21 Plus and a research grant (contract grant number 10040003) from the Ministry of Knowledge Economy of Korea.

REFERENCES

1. Novoselov, K. S.; Geim, A. K.; Morozov, S. V.; Jiang, D.; Zhang, Y.; Dubonos, S. V.; Grigorieva, I. V.; Firsov, A. A. *Science* **2004**, *306*, 666.
2. Geim, A. K. *Science* **2009**, *324*, 1530.
3. Kim, J. S.; Yun, J. H.; Kim, I.; Shim, S. E. *J. Ind. Eng. Chem.* **2011**, *17*, 325.
4. Wang, E.; Desai, M. S.; Lee, S. W. *Nano Lett.* **2013**, *13*, 2826.
5. Al-Hartomy, O. A.; Al-Ghamdi, A. A.; Al-Salamy, F.; Dishovsky, N.; Shtarkova, R.; Iliev, V.; El-Tantawy, F. *Int. J. Mater. Chem.* **2012**, *2*, 116.
6. Hernández, M.; Bernal, M. D. M.; Verdejo, R.; Ezquerra, T. A.; López-Manchado, M. A. *Compos. Sci. Technol.* **2012**, *73*, 40.
7. Singh, V.; Joung, D.; Zhai, L.; Das, S.; Khondaker, S. I.; Seal, S. *Prog. Mater. Sci.* **2011**, *56*, 1178.
8. Ozbas, B.; O'Neill, C. D.; Register, R. A.; Aksay, I. A.; Prud'homme, R. K.; Adamson, D. H. *J. Polym. Sci. Part B: Polym. Phys.* **2012**, *50*, 910.
9. Jing, X.; Mi, H.-Y.; Salick, M. R.; Peng, X.-F.; Turng, L.-S. *Polym. Compos.* **2014**, *35*, 1408.
10. Bora, C.; Gogoi, P.; Baglari, S.; Dolui, S. K. *J. Appl. Polym. Sci.* **2013**, *129*, 3432.
11. Tseng, I. H.; Liao, Y.-F.; Chiang, J.-C.; Tsai, M.-H. *Mater. Chem. Phys.* **2012**, *136*, 247.
12. Tang, J.; Zhou, H.; Liang, Y.; Shi, X.; Yang, X.; Zhang, J. *J. Nanomater.* **2014**, *2014*, 696859.
13. Scherillo, G.; Lavorgna, M.; Buonocore, G. G.; Zhan, Y. H.; Xia, H. S.; Mensitieri, G.; Ambrosio, L. *ACS Appl. Mater. Inter.* **2014**, *6*, 2230.
14. Allahbakhsh, A.; Mazinani, S.; Kalaee, M. R.; Sharif, F. *Thermochim. Acta* **2013**, *563*, 22.
15. Mao, Y.; Wen, S.; Chen, Y.; Zhang, F.; Panine, P.; Chan, T. W.; Zhang, L.; Liang, Y.; Liu, L. *Sci. Rep.* **2013**, *3*, 2508.
16. Kim, H.; Abdala, A. A.; Macosko, C. W. *Macromolecules* **2010**, *43*, 6515.
17. Kuila, T.; Bose, S.; Mishra, A. K.; Khanra, P.; Kim, N. H.; Lee, J. H. *Prog. Mater. Sci.* **2012**, *57*, 1061.
18. Ramanathan, T.; Abdala, A. A.; Stankovich, S.; Dikin, D. A.; Herrera-Alonso, M.; Piner, R. D.; Adamson, D. H.; Schniepp, H. C.; Chen, X.; Ruoff, R. S.; Nguyen, S. T.; Aksay, I. A.; Prud'homme, R. K.; Brinson, L. C. *Nat. Nanotechnol.* **2008**, *3*, 327.
19. Brodie, B. C. Philos. Trans. R. Soc. London **1859**, *149*, 249.
20. Stankovich, S.; Dikin, D. A.; Piner, R. D.; Kohlhaas, K. A.; Kleinhammes, A.; Jia, Y.; Wu, Y.; Nguyen, S. T.; Ruoff, R. S. *Carbon* **2007**, *45*, 1558.
21. Hummers, W. S.; Offeman, R. E. *J. Am. Chem. Soc.* **1958**, *80*, 1339.
22. Li, Y.; Wang, Q.; Wang, T.; Pan, G. *J. Mater. Sci.* **2011**, *47*, 730.
23. Mensah, B.; Kim, S.; Arepalli, S.; Nah, C. *J. Appl. Polym. Sci.* **2014**, *131*, 40640.
24. Young, R. J.; Kinloch, I. A.; Gong, L.; Novoselov, K. S. *Compos. Sci. Technol.* **2012**, *72*, 1459.
25. Porter, M. *Br. Polym. J.* **1990**, *23*, 359.
26. Flory, P. J.; Rehner, J. *J. Chem. Phys.* **1943**, *11*, 521.
27. Bristow, G. M.; Watson, W. F. *Trans. Faraday Soc.* **1958**, *54*, 1731.
28. Blake, P.; Hill, E. W.; Castro Neto, A. H.; Novoselov, K. S.; Jiang, D.; Yang, R.; Booth, T. J.; Geim, A. K. *Appl. Phys. Lett.* **2007**, *91*, 063124.
29. Bai, X.; Wan, C.; Zhang, Y.; Zhai, Y. *Carbon* **2011**, *49*, 1608.
30. Li, C.; Feng, C.; Peng, Z.; Gong, W.; Kong, L. *Polym. Compos.* **2013**, *34*, 88.

31. Shahriary, L.; Athawale, A. A. *Int. J. Renew. Energy Environ. Eng.* **2014**, *2*, 58.
32. Wang, H.; Robinson, J. T.; Li, X.; Dai, H. *J. Am. Chem. Soc.* **2009**, *131*, 9910.
33. Zheng, J.; Di, C.-A.; Liu, Y.; Liu, H.; Guo, Y.; Du, C.; Wu, T.; Yu, G.; Zhu, D. *Chem. Commun.* **2010**, *46*, 5728.
34. Das, A.; Chakraborty, B.; Sood, A. K. B. *Mater. Sci.* **2008**, *31*, 579.
35. Romasanta, L. J.; Hernandez, M.; Lopez-Manchado, M. A.; Verdejo, R. *Nanoscale Res. Lett.* **2011**, *6*, 508.
36. Zhan, Y.; Wu, J.; Xia, H.; Yan, N.; Fei, G.; Yuan, G. *Macromol. Mater. Eng.* **2011**, *296*, 590.
37. Yang, D.; Velamakanni, A.; Bozoklu, G.; Park, S.; Stoller, M.; Piner, R. D.; Stankovich, S.; Jung, I.; Field, D. A.; Ventrice, C. A., Jr.; Ruoff, R. S. *Carbon* **2009**, *47*, 145.
38. Lai, Q.; Zhu, S.; Luo, X.; Zou, M.; Huang, S. *AIP Adv.* **2012**, *2*, 032146.
39. Xu, S.; Yong, L.; Wu, P. *ACS Appl. Mater. Int.* **2013**, *5*, 654.
40. Liu, X.; Sun, D.; Wang, L.; Guo, B. *Ind. Eng. Chem. Res.* **2013**, *52*, 14592.
41. Shanmugharaj, A.; Bae, J.; Lee, K.; Noh, W.; Lee, S.; Ryu, S. *Compos. Sci. Technol.* **2007**, *67*, 1813.
42. Gudarzi, M. M.; Sharif, F. *Express Polym. Lett.* **2012**, *6*, 1017.
43. Nah, C.; Lim, J. Y.; Sengupta, R.; Cho, B. H.; Gent, A. N. *Polym. Int.* **2011**, *60*, 42.
44. Nah, C.; Lim, J. Y.; Cho, B. H.; Hong, C. K.; Gent, A. N. *J. Appl. Polym. Sci.* **2010**, *118*, 1574.
45. Rafiee, M. A.; Rafiee, J.; Srivastava, I.; Wang, Z.; Song, H.; Yu, Z.-Z.; Koratkar, N. *Small* **2010**, *6*, 179.
46. Stankovich, S.; Dikin, D. A.; Dommett, G. H. B.; Kohlhaas, K. M.; Zimney, E. J.; Stach, E. A.; Piner, R. D.; Nguyen, S. T.; Ruoff, R. S. *Nature* **2006**, *442*, 282.
47. Xu, Y.; Hong, W.; Bai, H.; Li, C.; Shi, G. *Carbon* **2009**, *47*, 3538.
48. Kang, H.; Zuo, K.; Wang, Z.; Zhang, L.; Liu, L.; Guo, B. *Compos. Sci. Technol.* **2014**, *92*, 1.
49. Affdl, J. C. H.; Kardos, J. L. *Polym. Eng. Sci.* **1976**, *16*, 344.
50. Liang, J.; Huang, Y.; Zhang, L.; Wang, Y.; Ma, Y.; Guo, T.; Chen, Y. *Adv. Funct. Mater.* **2009**, *19*, 2297.
51. Dai, G.; Mishnaevsky, L., Jr.; *Compos. Mater. Sci.* **2014**, *95*, 684.
52. Gomez-Navarro, C.; Burghard, M.; Kern, K. *Nano Lett.* **2008**, *8*, 2045.
53. Suk, J. W.; Piner, R. D.; An, J.; Ruoff, R. S. *ACS Nano* **2010**, *4*, 6557.
54. Tantis, I.; Psarras, G. C.; Tasis, D. *Express Polym. Lett.* **2012**, *6*, 283.
55. Dang, Z. M.; Wang, L.; Yin, Y.; Zhang, Q.; Lei, Q. Q. *Adv. Mater.* **2007**, *19*, 852.